



Politecnico  
di Torino



Université  
de Paris



SORBONNE  
UNIVERSITÉ

Master Program in  
NANOTECHNOLOGIES AND QUANTUM DEVICES

Politecnico di Torino | Université de Paris

Internship Report

---

# Quantum-Confined Mercury Telluride Nanocrystals and Their Application to Infrared Optoelectronics

---

Mariarosa Cavallo

Dr. Emmanuel Lhuillier

Tutor

Prof. Maria Luisa Della Rocca

Academic Advisor

Prof. Carlo Ricciardi

Academic Advisor

Institute des Nanosciences de Paris

March – June 2021

# Table of Contents

1	General context.....	1
1.1	Team.....	2
2	Introduction.....	2
2.1	Nanocrystals.....	2
2.2	Band gap and quantum confinement.....	3
2.3	Transport in Nanocrystals arrays.....	4
2.3.1	Hopping transport.....	4
2.3.2	Controlling the tunnel barrier.....	5
2.3.3	Field-effect transistors.....	6
2.4	Detection.....	7
2.4.1	Photodetection.....	7
2.4.2	Infrared detectors.....	8
2.5	Figures of Merits.....	8
2.6	Coupling to 2D materials.....	9
3	Results.....	10
3.1	Synthesis of QDs.....	10
3.1.1	Material characterization.....	11
3.2	Dual gated planar $p$ - $n$ Graphene/HgTe heterojunction.....	11
3.2.1	Fabrication.....	11
3.2.2	Characterization.....	12
3.2.2.1	FET measurements.....	13
3.2.2.2	I-V measurements.....	15
3.2.2.3	Time-response.....	18
4	Conclusion and perspectives.....	21
	Bibliography.....	22

# 1 General context

Infrared (IR) light is electromagnetic radiation invisible to the human eye, with wavelengths ranging from 800 nm to 300  $\mu\text{m}$ . Sensors operating above 3  $\mu\text{m}$  allow for passive thermal imaging in the dark, *i.e.*, to observe without the observer being detected. This has been of particular interest for defence applications, with a growing interest for many other implementations, such as in the industrial, commercial but also medical field.

The first implemented IR sensors in the 1950s were based on lead chalcogenides. Among many other candidate materials, InSb emerged as the most promising in the 3-5  $\mu\text{m}$  range. However, very narrow bandgap materials were needed to probe the targeted range of 8-12  $\mu\text{m}$ , corresponding to the peak of blackbody radiation emission at room temperature. Later in 1959, HgCdTe alloys emerged as photoconductive materials and are to date the most performing ones in the spectral range of 3-12  $\mu\text{m}$ . Other sensors are based on epitaxially grown quantum wells and type-II superlattices. However, these are all complex and expensive devices from the fabrication standpoint.

That's why, in the past twenty years, mercury chalcogenide<sup>[1]</sup> (HgX) Nanocrystals (NCs) have been widely studied and characterized for their use as active material in low-cost infrared optoelectronics. Quantum confinement in these nanoparticles has been shown to be the origin of the shift in the band gap energy: tunability of the absorption spectrum can be obtained by tuning the nanometric size of the particles. For HgTe, which is a semimetal in the bulk form, the absorption can be tuned from 1.5 eV to virtually zero. In practice, the smallest absorption feature has been obtained at 20 meV.<sup>[2]</sup> This constitutes a striking difference with respect to photoconductive materials based on alloys, where tunability of the bandgap comes from the content ratio of their components. Moreover, NCs are more easily produced and are more prone to batch fabrication than the epitaxially grown quantum wells.

Progress in material growth has led to size control<sup>[3,4]</sup> of the NCs: monodispersity is a key parameter in NCs syntheses. Indeed, by achieving narrower size distribution, energy dispersion of the discrete levels is reduced and the effect of quantum confinement is visible in an ensemble measurement.

Furthermore, recent progress in surface chemistry has allowed for the formation of high mobility HgX NCs films,<sup>[5,6]</sup> leading to an enhancement of IR detectors performances.

Still, advancement in several aspects is needed to further improve performance, maximize signal-to-noise ratio and speed up the photoresponse time. The need for such improvements has led to a variety of designs for IR detectors, ranging from photoconductive<sup>[7,8]</sup> to photovoltaic<sup>[9,10]</sup> devices. Among these, NCs have been coupled to 2D materials,<sup>[11,12]</sup> such as graphene,<sup>[13]</sup> first with the idea of enhancing the limited mobility of the NCs arrays, whose transport relies on hopping mechanisms. By using graphene for its large carrier mobility as a channel, it could be possible to generate gain, thus improving the responsivity. Some fundamental limitations were however met, and the interest shifted toward the use of graphene as a transparent conductive contact instead. Concept, evolution and improvements of device geometries based on this idea will be presented later in the report.

### 1.1.1 Team

The Optoelectronic of Confined Nanomaterials (OCN) group is part of the Institute des Nanosciences de Paris (INSP) from Sorbonne Université, the laboratory in which the internship took place. The team’s research is focused on the investigation of colloidal nanocrystals and 2D materials with the aim of correlating the nanomaterial structural properties to the transport properties and electronic structure as well.

The team specializes in the synthesis of narrow band gap semiconductors and semimetal NCs for their transitions in the IR. Transport properties of the obtained films are studied as well as their gating methods. The aim is to develop and fabricate cost effective infrared detectors.

Clean room fabrication of the devices, glove box processing and device characterization are all performed in the laboratory.

## 2 Introduction

During my internship, I was involved in a broad variety of tasks. However, for the sake of consistency, the report will be focused on one particular subject: the fabrication and characterization of a SWIR (short-wave infrared) sensor in which an heterostructure made of a film of NCs and a graphene layer is implemented on a split-gate Field Effect Transistor architecture, to speed up the photoresponse.

This first part of the report aims at introducing the general concepts linked to NCs—fundamental for the understanding of the topic—and their state of the art. In the second part, results obtained during the internship are presented and discussed.

### 2.1 Nanocrystals

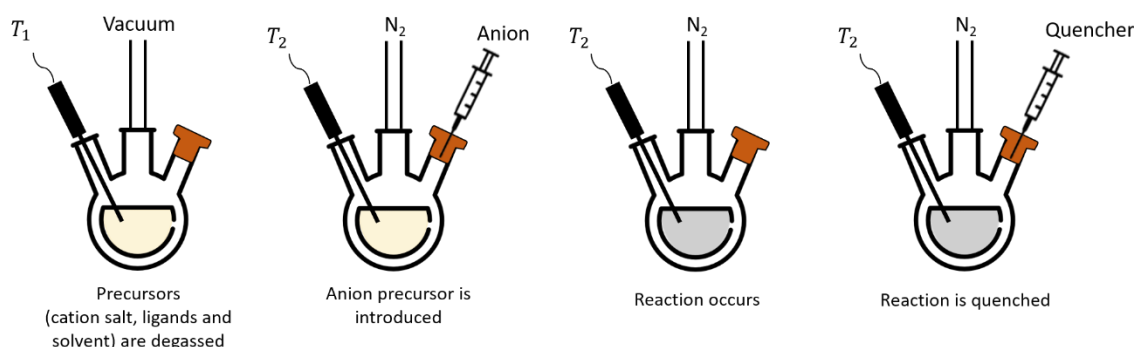


**Figure 2.1:** General procedure for nanocrystals syntheses.

Colloidal semiconductor nanocrystals (NCs) are nanometer sized crystals of semiconductors. In 1993 Murray, Norris and Bawendi presented a synthesis of nearly monodisperse II-VI nanocrystals of CdE (E = S, Se, Te).<sup>[14]</sup> Considerable progress in terms of shape and composition control has been made since then, making such structures already available for mass market as green and red downconverters for LCD displays.

The current synthesis of HgX nanocrystals follows the Keuleyan’s procedure<sup>[15]</sup> in which the cation salt (HgCl<sub>2</sub>), ligands and solvent, are introduced in a three neck flask (see [Figure 2.1](#)). They are degassed under vacuum to remove oxygen and water, thus preventing oxidation. Then, the atmosphere is switched to a neutral gas (generally N<sub>2</sub>)

and the content of the flask is heated to a certain temperature which depends on the material (from 60 to 120°C in the case of HgTe). The anion is then introduced and the reaction starts. Once the targeted size of the nanocrystals is reached, the reaction is quenched by adding ligands and cooling down.

The unreacted species and the solvent are then removed by precipitation. This important step in the synthesis process is carried out by adding a polar solvent (such as (m)ethanol) to the nanoparticle solution and centrifugating: a pellet forms at the bottom, due to the aggregation of the precipitated nanoparticles, and the above supernatant is discarded. Finally, the pellet is redispersed in an apolar solvent (such as toluene) and the final solution is obtained.

Surface ligands (surfactants) are what makes colloidal quantum dots (CQDs) different from their epitaxially grown counterpart. They are usually long alkyl chains (C<sub>12</sub> to C<sub>18</sub>) with a an organic function (thiol : SH, in the case of HgTe) at their tip which will bond to the NC surface. Their role consists in (i) slowing down the reaction, thus ensuring that crystal growth is slow to keep it with a size below or around Bohr radius; (ii) they ensure a certain spatial separation between the NCs, preventing aggregation and increasing solution stabilization; (iii) they passivate the surface through hybridization with dangling bonds.<sup>[16]</sup>

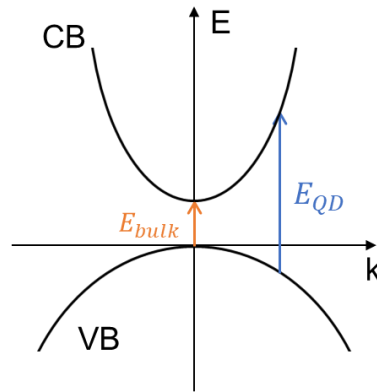


**Figure 2.2:** Semiconductor band diagram scheme.

## 2.2 Band gap and quantum confinement

The nanoparticles grown with the previously explained method have a size which is in the range of (3 - 20) nm. At such small scales, quantum confinement effect can be observed: this occurs when the size of the nanoparticles is smaller than the Bohr radius, a physical constant depending on the exciton effective mass  $\mu$  and on the dielectric constant of the material  $\epsilon_r$  :

$$a_0 = \frac{4\pi\epsilon_0\epsilon_r\hbar^2}{m_0\mu e^2}$$

Where  $\epsilon_0$  is the vacuum permittivity,  $\hbar$  the reduced Planck's constant,  $m_0$  the mass and  $e$  the electron charge. For HgTe nanocrystals, the Bohr radius is 40 nm, therefore all particles having a size smaller than 40 nm are confined.

Confinement has two direct consequences: (i) nanocrystals, or quantum dots (QDs), have a discrete density of states and (ii) the finite size makes the central part of the Brillouin Zone unavailable, since the wavevector  $k$  scales like the inverse of the particle

size. From the latter the band gap originates, given by the sum of the bulk band gap  $E_{bulk}$  (which is zero for HgTe) and the electron and hole confinement energies (see Figure 2.2). Consequently, tunability originates from size shrinking of the NCs.

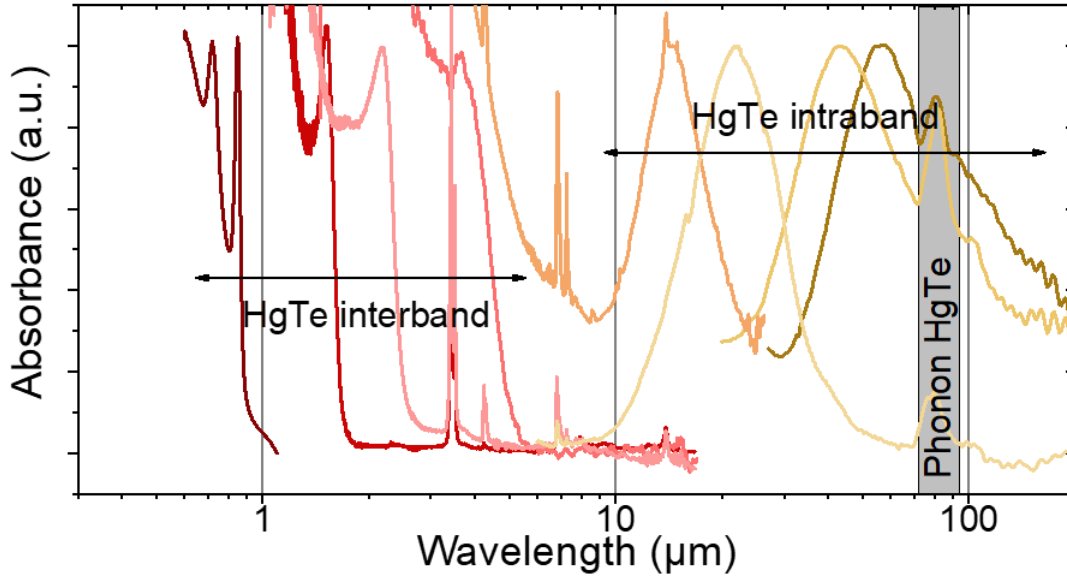


**Figure 2.3:** Absorption spectra for various sizes of HgTe NCs.

HgTe NCs, among other semiconductor NCs,<sup>[1]</sup> show the broadest spectral tunability, covering wavelengths from 1  $\mu\text{m}$  to 100  $\mu\text{m}$  (see Figure 2.3). This is linked to the semimetal nature (*i.e.*, lack of bulk band gap) of the bulk HgTe: a very narrow band gap can be designed thanks to confinement, allowing for absorption of IR radiation. In this case, the optical absorption involves a transition between the valence and the conduction band: it is an *interband transition*. However, there is a different type of transition, called *intraband*, which can take place within a single band (usually the conduction band): this transition is narrower in energy, allowing to access optical absorption at even higher wavelengths (higher than 5  $\mu\text{m}$ ). For this type of transition to occur within the conduction band, the material needs to be doped in order to introduce electrons in the conduction band.

## 2.3 Transport in Nanocrystals arrays

### 2.3.1 Hopping transport

The transport mechanism in NCs films occurs through *hopping*: charges have to hop from one nanocrystal to the other in order to contribute to conduction. In this type of transport, the ground state of each NC has an associated wavefunction which weakly overlaps with that of the neighbouring crystals. The latter directly relates to the height and length of the tunnel barrier formed by the capping ligands (see Figure 2.4). Charge transfer occurs via tunnel effect from one ground state to the other, and the process may also be assisted by phonons at high temperature.

The tunnel barrier is the key parameter driving the carrier mobility. One can write the transparency of the barrier as<sup>[17]</sup>:

$$T = \exp\left(-2l \sqrt{\frac{2m^*V_B}{\hbar^2}}\right) = \exp(-\beta l)$$

Where  $l$  is the barrier length,  $V_B$  the barrier height and  $m^*$  the effective mass of the carrier.  $\beta$  describes the extension of the wave-function in the barrier, with a typical value of  $1\text{\AA}^{-1}$  in NCs films.<sup>[18]</sup> Mobility can be written using a diffusive model, through Einstein's equations. By considering each hopping step as a tunnel event and introducing the activation energy of the hopping process  $E_{A,\mu}$  one obtains the mobility for one channel, which can be written as

$$\mu = \frac{eR^2}{3hk_B T} \exp\left(-\beta l - \frac{E_{A,\mu}}{k_B T}\right)$$

Where  $\mu$  is the charge mobility,  $R$  the nanocrystal size and  $k_B T$  is the thermal energy. The activation energy of the mobility is generally low, in the order of a few tens of meV, and much weaker than the activation energy of the carrier density  $E_{A,n}$ .

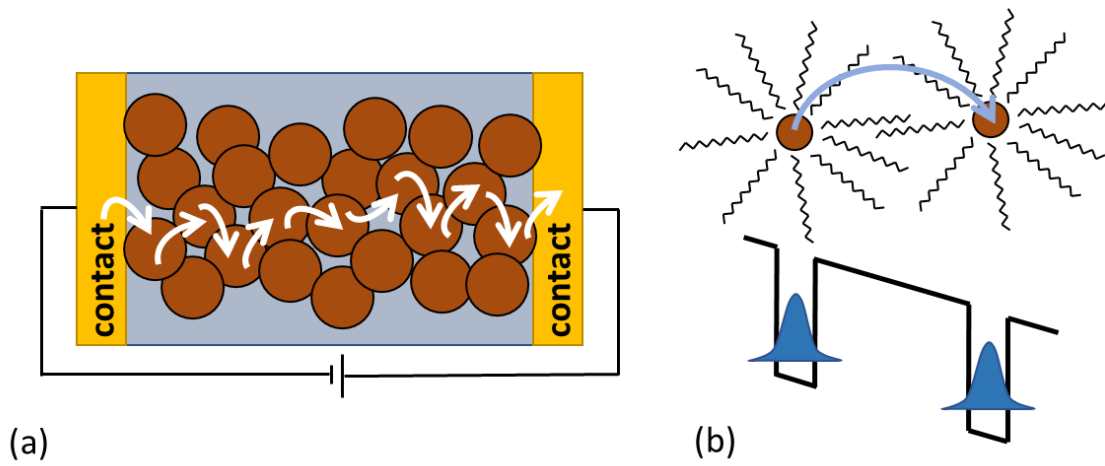


**Figure 2.4:** a. Hopping transport in a nanocrystal film. b. Two neighbour nanocrystals separated by long ligands, which form a barrier.

Considering a NC film between two electrodes, transport is driven by the hopping events from one contact to the other: the number of hopping steps depends on the spacing between the two electrodes. Charge transport is therefore a diffusive process, and transport itself is susceptible to change with current, temperature and film aging.

An important factor contributing to transport is also size dispersion in the nanocrystal population: as already mentioned, to a different size corresponds a different band gap. A bigger NC has a narrower band gap, meaning that a carrier arriving in this site will tend to stay longer, since a much higher barrier has to be overcome. Bigger-than-average NCs will therefore act as trap states, and polydispersity will lead to a lower carrier mobility.

### 2.3.2 Controlling the tunnel barrier

Ligands capping the NCs define the length and height of the tunnel barriers. Control of the barrier can then be performed by ligand exchange procedures, in which the long ligands (dodecanethiol, DDT) are replaced by shorter ones, effectively reducing the size of the barrier (as shown in [Figure 2.5](#)) and enhancing the conductivity.<sup>[18]</sup> Two different approaches can be used.

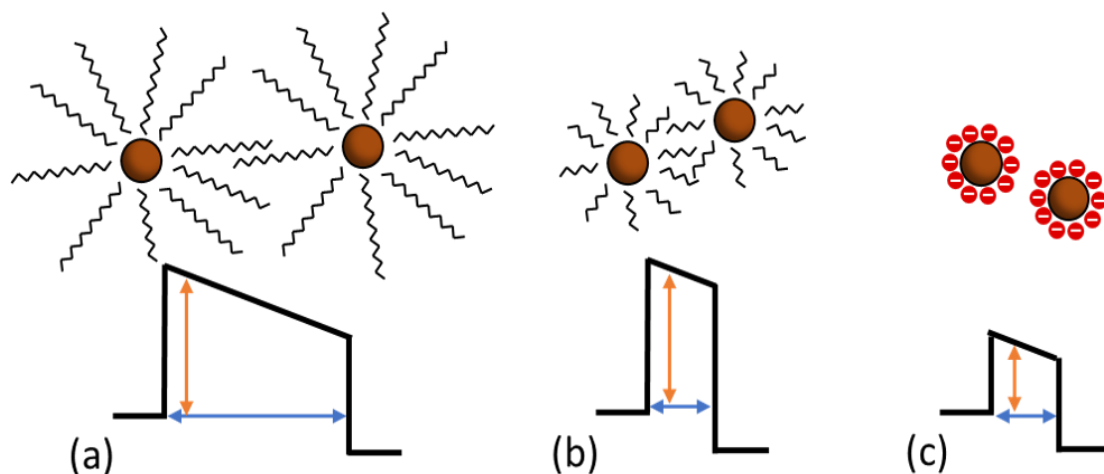


**Figure 2.5:** Effect of the capping ligands on the interparticle tunnelling barrier. a. long alkane chains (DDT). b. short alkane chains (e.g., EDT). c. ion-capped NCs.

*Solid-state ligand exchange* is performed at the film level: the film of NCs is dipped in the ligand exchange solution, which is typically 0.1% (in volume) of ethanedithiol (EDT) in a polar solvent such as ethanol. As ligand exchange occurs, the volume of the particles is reduced because the long ligands are exchanged for shorter ones. This leads to a strong volume reduction of the film: cracks are induced in the film and if the film is thick, too many cracks appear. That's why the procedure is efficient only on thin films (<50 nm), and a multilayer deposition is needed, both to obtain a thicker film and to fill the cracks. Usually, at least ten deposition steps are needed to reach a final film thickness of 200 nm.

An alternative and more recent procedure, developed only after 2010,<sup>[19,20]</sup> is *liquid-phase ligand exchange* in which the NCs initially dispersed in a non-polar solvent are mixed with a polar phase containing short ionic ligands. The native long ligands are therefore replaced by short ones and the NCs become soluble in the polar phase. This process leads to the so-called *ink*, which can be directly deposited into a thicker film without further post-processing.<sup>[21]</sup>

### 2.3.3 Field-effect transistors

The best way to evaluate mobility in the NCs films is to use a Field Effect Transistor (FET) geometry, which also allows for the determination of the majority carriers within the NCs film.

Gating of the FET can be implemented in many different ways. One involves the use of silica (or alumina) on silicon as dielectric to design a back gate FET (Figure 2.6a); however, they are limited in gate capacitance and the gate effect is efficient only for thin NCs films.

Alternative geometries implement electrolyte gating to design a top gate FET<sup>[22,23]</sup> (Figure 2.6b). An electrolyte is made of ions, which are lithium and perchlorate ions ( $\text{Li}^+$ ,  $\text{ClO}_4^-$ ) in our case, dispersed within a liquid or a polymer, such as polyethylene glycol (PEG). The  $\text{Li}^+$  ions percolate in the film when a positive gate bias is applied. In turn, the electrodes inject negative carriers in the NCs film to screen the positive charges. Higher capacitances than in dielectrics are achieved thanks to ions percolation. Gate effect in thick NCs film can be obtained.

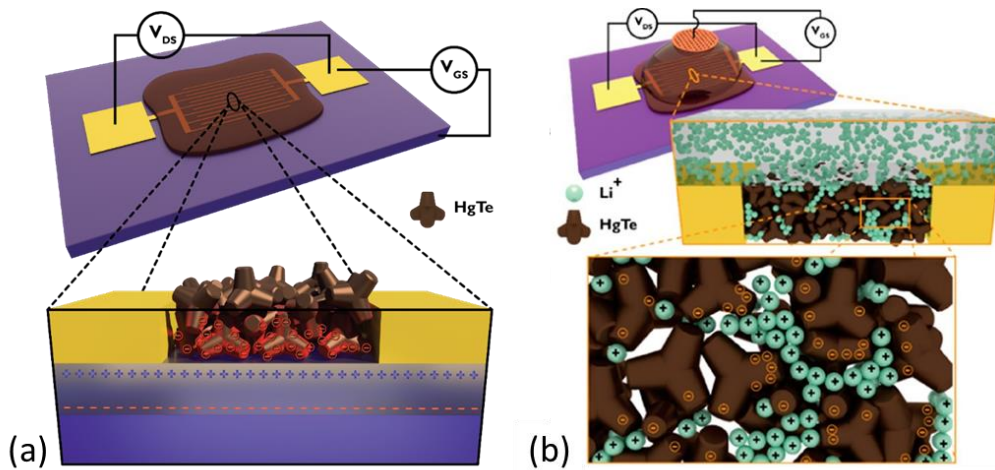


**Figure 2.6:** Possible gating solutions: a. Back gate FET on dielectric. b. Top gate FET with an electrolyte.

## 2.4 Detection

### 2.4.1 Photodetection

Photodetectors transduce the optical absorption into an electric signal. Different strategies have been developed, based on geometries which are either planar or vertical (Figure 2.7).

Photoconductors are often based on planar geometries, and have been refined with phototransistors<sup>[24]</sup> and coupling to 2D materials.<sup>[12]</sup>

Phototransistors are planar geometries in which the photoconductive film is also a FET. The advantage of this geometry comes from the presence of the gate, which allows tunability of the photoresponse, by controlling the majority carrier density. Furthermore, to the planar geometry is associated a reduced capacitance, which induces a shorter RC time constant, as will be discussed later.

Vertical stacks, as in photovoltaic devices,<sup>[25]</sup> rely on heterostructures to create *p-n* junctions. A transparent conductive oxide, such as fluorine-doped tin oxide (FTO) or tin doped indium oxide (ITO), is used as the bottom contact to allow illumination of the heterojunction. Then n-type and p-type NC films are deposited. To favour current flow, an Electron Transport Layer (ETL) and a Hole Transport Layer (HTL) are employed on both sides of the *p-n* junction. A drawback associated to these devices, which are thin, is the large sheet capacitance, given by  $\epsilon/d$  with  $\epsilon$  the dielectric constant and  $d$  the thickness.

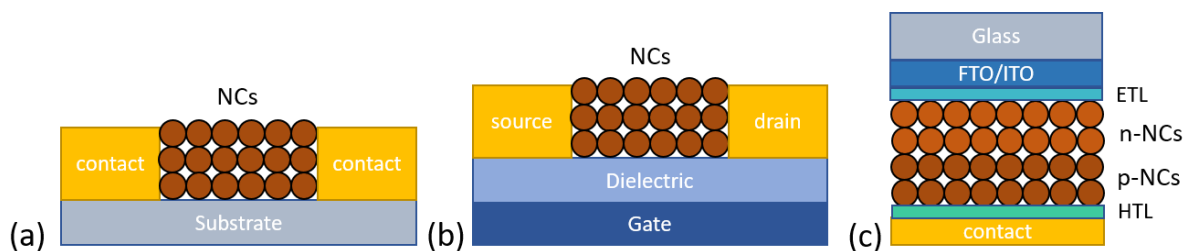


**Figure 2.7:** Scheme of a photoconductor (a), phototransistor (b) and photodiode (c).

### 2.4.2 Infrared detectors

There are two different types of IR detectors: thermal detectors, which detect an energy flux, and photodetectors, which detect a photon flux. The former has an active material that converts into heating the absorbed infrared light. Examples are bolometers, which make use of a temperature-dependent resistance. They are used in thermal detectors and cameras, for their relatively low-cost.

Photodetectors, also called quantum detectors, are based either on transitions between the valence band and conduction band (interband) or within a band (intraband). When an infrared photon is absorbed, an electron-hole pair (or *exciton*) is generated: the charges move under the influence of an electric field, contributing to the photocurrent. The optical transitions occur at the energy of the infrared photon, which is very low. When this energy is comparable to the thermal energy  $k_B T$ , a non-negligible number of excitons is generated by thermally activated processes, contributing to dark current. Therefore, cooling down to reduce the thermal activation and thus the dark current is needed. This increases the overall cost of the infrared quantum detectors.

## 2.5 Figures of Merits

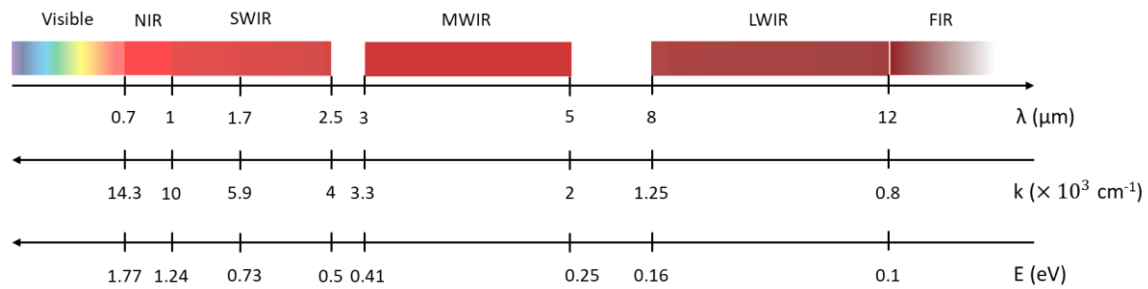


**Figure 2.8:** Infrared spectrum.

When targeting to compare different types of IR photodetectors, figures of merits are required.

**Spectral response** The infrared range covers a wide range of wavelengths, which can be subdivided in three main regions: the near-infrared, mid-infrared and far-infrared regions. In sensing, the subdivision is even finer (Figure 2.8):

- Near infrared (NIR) has wavelengths ranging from 700 to 900 nm;
- Shortwave infrared (SWIR) spans from 1 to 1.7  $\mu\text{m}$ , but it can also be extended up to 2.5  $\mu\text{m}$  (E-SWIR);
- Mid-wave infrared (MWIR) goes from 3 to 5  $\mu\text{m}$ ;
- Longwave infrared (LWIR) from 8 to 12  $\mu\text{m}$ , matching the black body emission at 300 K;
- Far infrared (FIR) from 12  $\mu\text{m}$  to 100  $\mu\text{m}$ ; this region overlaps with the Terahertz range (THz).

The *spectral response* describes the sensitivity of the photodetectors to radiations of different wavelengths.

**Responsivity** *Responsivity* ( $R$ ) gives a measure of the input-output gain of a material and it relates to its ability to convert the incident optical power ( $P_{in}$ ) into an electrical signal, called photocurrent ( $I_{ph}$ ). It is given by the ratio

$$R = \frac{I_{ph}}{P_{in}}$$

and it is measured in  $A \cdot W^{-1}$ .

**Noise Equivalent Power and Specific Detectivity** The *Noise Equivalent Power* (NEP) is expressed as the ratio between the current noise spectral density ( $\delta I_n$  in  $A \cdot Hz^{-1/2}$ ) and the responsivity ( $R$ ):

$$NEP = \frac{\delta I_n}{R}$$

and it is measured in  $W \cdot Hz^{-1/2}$ . It is an indicator of the availability to detect the minimum illumination power. The lower the value, the better the photodetector.

Another way to express the NEP is the *Specific Detectivity* ( $D^*$ ) which is the inverse of the NEP normalized by the optical area of the device:

$$D^* = \frac{\sqrt{A \cdot f}}{NEP}$$

With  $f$  the bandwidth. It is measured in  $cm \cdot Hz^{1/2} / W$  or Jones.

**Response time** It gives a measure of how fast the detector's response to light absorption is. For their application in imaging sensors, the response time has to be fast (smaller than  $1/25$  s) to be compatible with video frame rates (25 fps). To measure it, a pulsed source is shined on the detector.

**Operation temperature** Cooling down of detectors is needed to reduce the dark current and increase the signal-to-noise ratio. However, this increases the cost/weight and volume of the detectors.

## 2.6 Coupling to 2D materials

As previously explained, transport in NCs films occurs via a hopping mechanism, which leads to low carrier mobilities. This is why, already 10 years ago, Konstantatos *et al.*<sup>[13]</sup> first proposed to couple PbS NCs to graphene, with the idea of enhancing the mobility of the NCs arrays. The device exploited photoconduction gain<sup>[26]</sup> to achieve large responsivities ( $>10^6 A \cdot W^{-1}$ ). Photoconduction gain is the recirculation process by which, after the generation of an electron-hole pair, one type of carrier is transferred to graphene while the other is trapped in the NC array, according to the band alignment between the two materials. As long as the second type of carrier is trapped in the NCs film, the first type will recirculate in graphene to ensure neutrality of the whole structure. This means that carriers will not recombine, effectively generating gain, *i.e.*, more than one electron per absorbed photon. The use of graphene, with its high mobility, allowed to accelerate the recirculation process. Later, the same concept was applied to HgTe NCs<sup>[27]</sup> to push the spectral response.

However, two main limitations were introduced by graphene/QD heterostructures: high dark current, due to the high carrier density of graphene resulting from the lack of

band gap, and extremely slow response time, resulting from the transfer mechanism of the charge carrier from the NC to the graphene. This explains why graphene has no longer been used as a channel for its high mobility but rather as an electrode, exploiting its optical transparency to light and electric field. Since graphene is extremely thin, it allows the gate-induced electric field to penetrate through it and modulate the electronic states of the photosensitive film deposited on its surface.<sup>[12]</sup>

### 3 Results

#### 3.1 Synthesis of QDs

During the internship, I learned how to perform syntheses of HgTe NCs with bandgaps around  $4000\text{ cm}^{-1}$  (0.5 eV) and  $6000\text{ cm}^{-1}$  (0.74 eV), called respectively “HgTe 4k” and “HgTe 6k”. These syntheses follow the general procedure reported in the introduction chapter. Here, the detailed protocol for HgTe 4k is presented.

**HgTe 4k:** In a 100 mL three-neck flask, 543 mg of  $\text{HgCl}_2$  and 50 mL of oleylamine (OLA) are degassed under vacuum at  $110^\circ\text{C}$  for one hour. Meanwhile, 2 mL of tri-octylphosphine:Telluride (TOP:Te) (1 M) precursor solution are extracted from the nitrogen-filled glove box, in which they are stored, and mixed with 9 mL of OLA. After switching the atmosphere to  $\text{N}_2$  and stabilizing the temperature at  $82^\circ\text{C}$ , the TOP:Te solution is quickly injected. After 2'30", 10 mL of a mixture of DDT in toluene (10% of DDT) are injected and the temperature is quickly decreased by a water bath to quench the reaction. The content of the flask is split over 4 tubes and methanol (MeOH) is added. After centrifugation, the formed pellets are redispersed in one tube with toluene. The solution is precipitated a second time using ethanol. Again, the formed pellet is redispersed in toluene. At this step, the nanocrystals are centrifuged in pure toluene to get rid of the lamellar phase. The solid phase is discarded, while the stable phase is transferred in a weighted falcon and finally precipitated using MeOH. The solid is dried under vacuum for 30 min (in the glove box vacuum chamber). Finally, nanocrystals are redispersed with a  $50\text{ mg}\cdot\text{mL}^{-1}$  concentration in toluene.

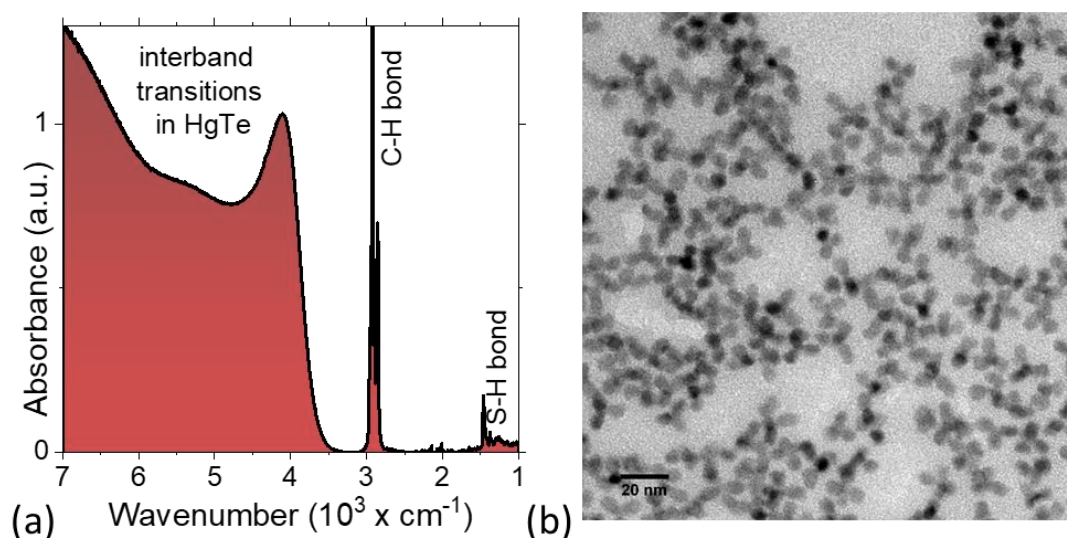


**Figure 3.1:** a. Absorption spectrum of HgTe NCs with a cut-off wavenumber of  $4000\text{ cm}^{-1}$ . b. TEM image of these NCs.

### 3.1.1 Material characterization

To make sure that the synthesis leads to the targeted result, an absorption spectrum is measured by Fourier Transform Infrared Spectroscopy (FTIR), as the one shown in [Figure 3.1](#). The bandgap is extrapolated by locating the onset of the transition peak, which is broad and whose position depends on the size of the quantum dots. Another peak, much narrower, is always present in the spectrum at around  $2900\text{ cm}^{-1}$  and corresponds to the C-H bond resonance from the DDT ligands.

## 3.2 Dual gated planar $p$ - $n$ Graphene/HgTe heterojunction

The presence of trap states in NCs films is at the origin of the slow response time observed in NC-based devices, due to the slow carrier release from them. Even though development of new surface passivation has led to a reduced number of traps while increasing the coupling between NCs, obtaining devices with fast response times remains challenging. Indeed, currently, most devices based on HgTe NCs present a time response in the 100 ns (for photodiodes) to few  $\mu\text{s}$  range. This is not compatible with some applications, such as Light Detection and Ranging (LiDAR) sensing, in which operations as fast as 10 or even 100 MHz of frequencies are required.

With the goal of obtaining faster response times, a new device geometry was conceived by the team, by combining two previously designed geometries. The first one implemented a single large capacitance gate and graphene as source and drain electrodes,<sup>[12]</sup> while the second implemented two back gates and metal source/drain electrodes.<sup>[28]</sup>

The main features of this device are:

1. The planar geometry of a FET, to which is associated a lower capacitance with respect to photovoltaic devices made of vertical stacks;
2. The presence of two separate back gates, which allow to control independently the carrier concentration on each side of the junction;
3. Source and drain electrodes made of graphene, which has a gate tunable work-function and is largely transparent to the electric field induced by the gates, since graphene is thinner than its Thomas-Fermi screening length.

This last feature implicates that the  $p$ - $n$  junction induced by the gates can propagate in the NCs film, enhancing the area over which charge dissociation occurs. Combined with the other two features, faster response times can be expected.

### 3.2.1 Fabrication

Fabrication of the Split Gate photodiode based on Graphene/HgTe NCs was performed by members of the team in collaboration with the IPCMS group at Université de Strasbourg. The device is shown in [Figure 3.2](#). Sang-Soo Chee, a post-doc at INSP, fabricated the bottom part of the device, in which gate electrodes and source/drain pads are patterned onto a Silicon on Silica substrate by consecutive metal deposition of Chromium, Gold and Aluminium. Then  $\text{Al}_2\text{O}_3$ , the gate dielectric, is deposited by Atomic Layer Deposition (ALD).

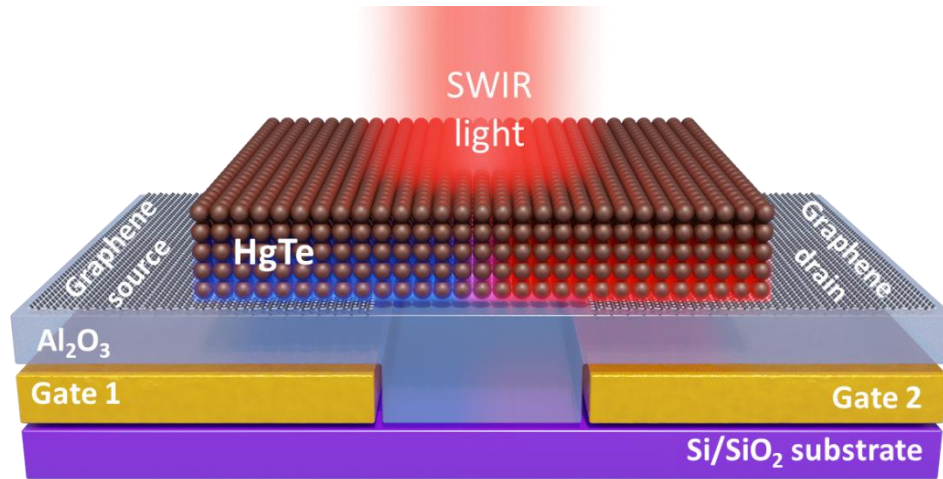


**Figure 3.2:** Schematic of the dual gated planar  $p$ - $n$  graphene/HgTe heterojunction.

The Graphene drain and source electrodes were fabricated from monolayer graphene grown by chemical vapor deposition (CVD). This part was performed by the team of Jean-Francois Dayen at IPCMS.

Then the HgTe layer is deposited on the device to create the HgTe NC channel. The ink was prepared by me under the supervision of Charlie Gréboval, a PhD of the team, starting from a HgTe 4k solution ( $E_g = 0.5$  eV), according to the following procedure: first, the ligand exchange solution is prepared by dissolving 15 mg of  $\text{HgCl}_2$  in 9 mL of DMF and adding 1 mL of mercaptoethanol (MPOH). Then, 500  $\mu\text{L}$  of NC solution at 50  $\text{mg}\cdot\text{mL}^{-1}$  is mixed with 5 mL of hexane. 1 mL of the previously prepared ligand exchange solution is added and mixed vigorously. NCs undergo a phase transfer from the apolar phase to the polar phase, helped by adding 1 mL of fresh DMF. The apolar phase is removed, and another cleaning step is performed. Then, few drops of toluene are added and the NCs are precipitated. Finally, they are redispersed in DMF at a concentration of 160  $\text{mg}\cdot\text{mL}^{-1}$ .

To obtain the film, 15  $\mu\text{L}$  of ink solution are spin-coated on the substrate at 1200 rpm for 120 s and then dried at 2500 rpm for 60 s. Before performing the spin-coating on the device, a test of the spin-coating recipe is done on a piece of glass, in order to probe film homogeneity and to measure the actual thickness of the film by profilometer.

### 3.2.2 Characterization

My main contribution during the internship activity was characterization of the devices and data analysis.

For the dual gated planar  $p$ - $n$  Graphene/HgTe NC heterojunction, a full characterization of the device required the following measurements:

- Transfer curves (drain and gate currents as a function of the applied gate voltage) at different temperatures and temperature dependence of the dark current;
- I-V curves in dark and under illumination at different temperatures;
- Photocurrent map as a function of the applied gate biases;
- Time-response measurements.

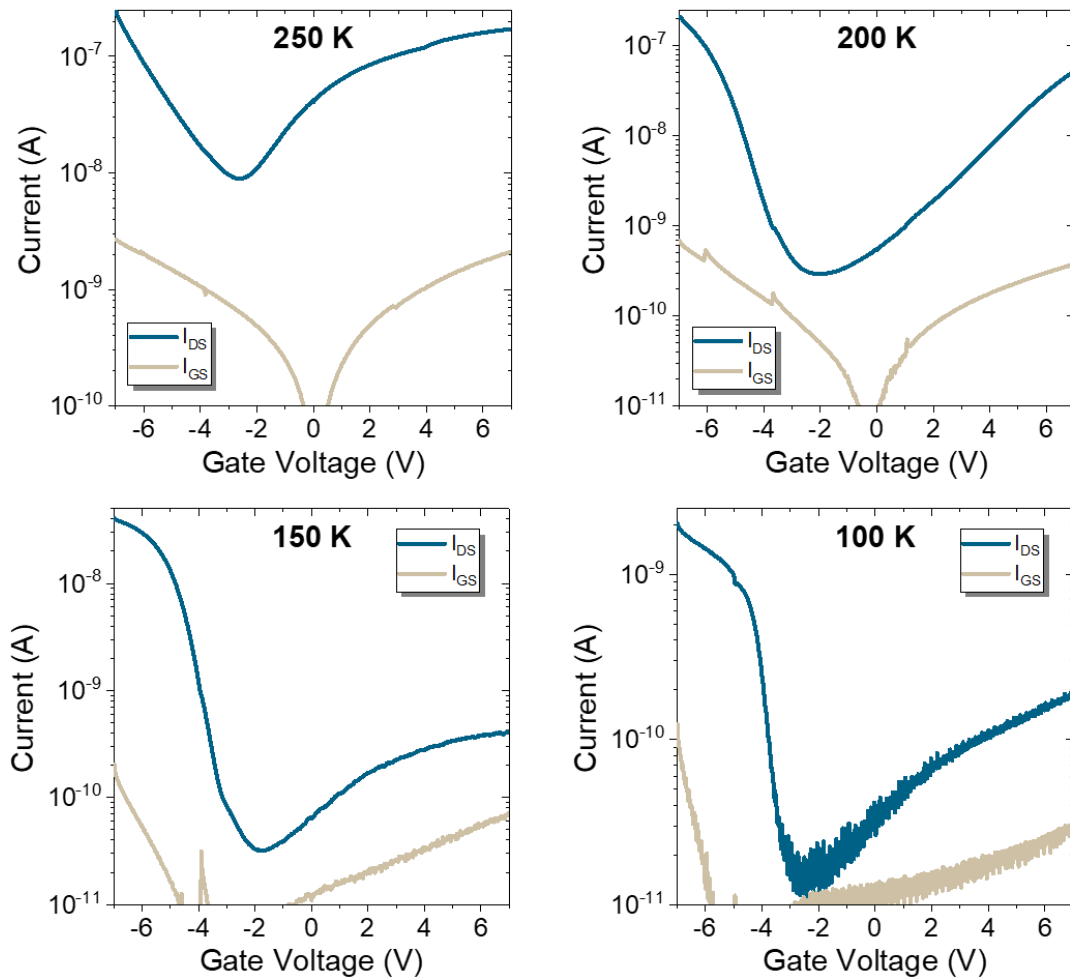


**Figure 3.3:** Transfer curves (drain-source and gate-source currents as a function of the gate bias) at 250 K, 200 K, 150 K and 100 K. In this case the two gates are connected together.

To perform these measurements, the sample was mounted on the cold finger of a closed cycle He cryostat. The two gates are connected to the two channels of a sourcemeter (Keithley 2634B) while the drain source electrodes are connected to another Keithley 2634B which is used to apply a channel voltage and measure the resulting current.

### 3.2.2.1 FET measurements

**Transfer curves** show drain-source current (and gate-source current) as a function of the gate bias. Here, the two gates are connected together. What these curves allow to determine is whether the film is conductive or not and, most importantly, which type of carriers contribute most to conduction. For this measurement the gate bias is varied from -7.0 V to 7.0 V and the current is measured, by means of an ad-hoc created LabVIEW sequence.

In this device, an ambipolar behaviour of the NCs film is required to later induce a  $p$ - $n$  junction: both  $p$  and  $n$  carriers are needed at the opposite side of the junction. Indeed, the obtained curves shown in [Figure 3.3](#) are in accordance with what's expected: the film conducts both electrons and holes, since both branches are visible (on right and left,

respectively). One also sees that the hole branch has a higher contribution, implying a higher hole mobility. The neutrality point is located on the negative polarity side, at  $V_N = -1.75$  V.

It is interesting then to notice how the behaviour changes when varying the temperature. The amplitude of the off-current decreases as the temperature decreases, going from  $10^{-8}$  to  $10^{-11}$  A. This drop can be related to the presence of less thermally activated carriers.

An important parameter to be evaluated is the activation energy for the dark current: it tells us at which temperature the device can be operated and how much improvement in terms of performance can be obtained by cooling down. In an infrared-sensing device, dark current is due to the thermally activated majority carrier density and can be expressed by the Arrhenius equation:

$$I_{dark}(T) \propto \exp\left(-\frac{E_{A,n}}{k_B T}\right)$$

Where  $E_{A,n}$  is the activation energy for the majority carrier density,  $k_B$  the Boltzmann constant and  $T$  the temperature. By experimentally measuring the evolution of the dark current as a function of temperature, it is possible to extract the activation energy by fitting the curve with an exponential function. With the temperature varying from 300 K to 100 K, the value of the current in the dark and under 1 V channel bias is recorded. The obtained curve, shown in Figure 3.4, is plotted as a function of  $1000/T$ . By fitting with the function  $y = A_1 \exp(-x/t_1)$  the activation energy is easily calculated as:

$$E_{A,n} = \frac{(k_B \times 1000)}{t_1} \approx \frac{0.086}{t_1}$$

Where  $k_B$  is expressed in  $\text{eV} \cdot \text{K}^{-1}$ , so that the obtained activation energy is given in eV. For this set of data, the activation energy was found to be  $E_{A,n} \approx 160$  meV, which is smaller than half of the bandgap  $E_g/2 \approx 250$  meV, the value expected for an intrinsic semiconductor. This is consistent with the position of the neutrality point observed in the FET measurements.

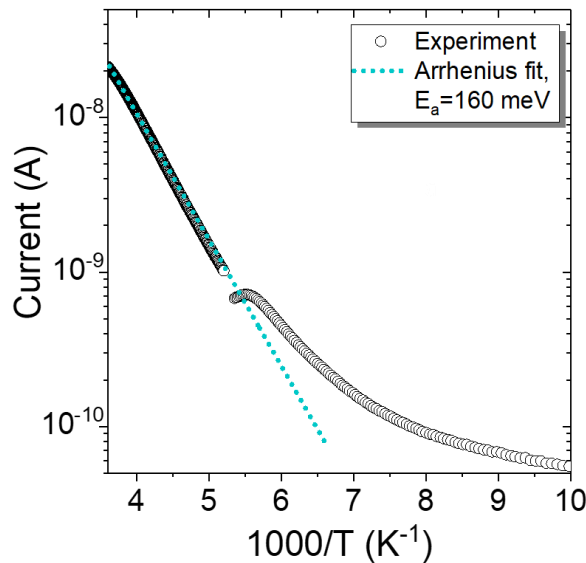


**Figure 3.4:** Temperature dependent current and Arrhenius fit.

### 3.2.2.2 I-V measurements

After having ascertained the ambipolarity of the NCs film, the goal is then to induce a certain carrier density profile by varying the applied gate bias, in order to drive the system into different operating modes. To see whether the targeted goal has been obtained or not, **I-V curves** must be measured: they are evidence of a certain device operation. When the two gates are operated with the same bias, the system behaves as a single gated FET, resulting in identical doping on both sides of the junction. In this case, the expected I-V curve is linear and symmetric. Instead, when the two gates are operated with opposite bias, two different and opposite doping profiles are obtained on the two sides of the junction. These opposites carrier densities form a *p-n* junction, whose signature in an I-V measurement is the rectifying behaviour.

In order to see this, the applied channel bias is tuned from -1 V to 1 V and the measurement is repeated at four different gate biases configurations:

- $V_{G1} = V_{G2} = 6 \text{ V}$
- $V_{G1} = -6 \text{ V}; V_{G2} = +6 \text{ V}$
- $V_{G1} = +6 \text{ V}; V_{G2} = -6 \text{ V}$
- $V_{G1} = V_{G2} = -6 \text{ V}$

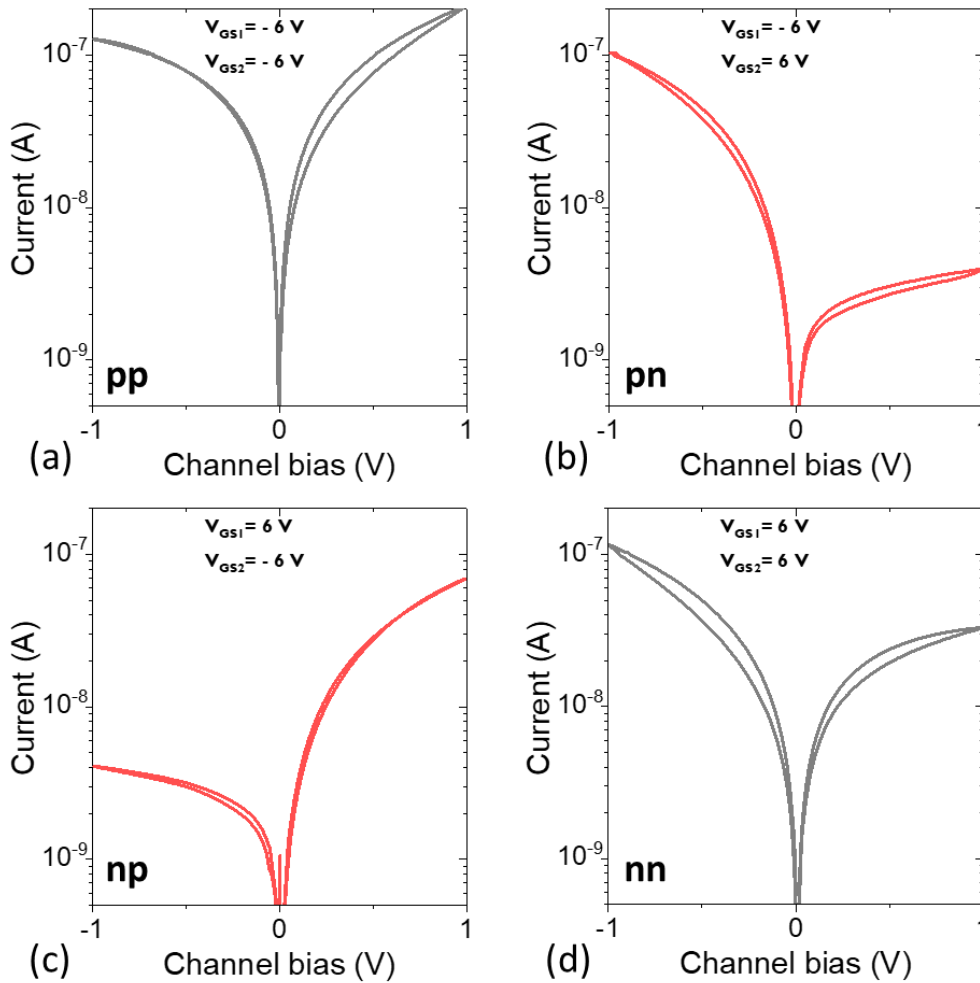


**Figure 3.5:** I-V curves for four different gate bias configurations, measured at 250 K. a and d. Same gate voltages (transistor mode). b and c. Opposite gate voltages (diode mode).

The obtained curves at 250 K are shown in Figure 3.5. The two operation modes of the device are clearly distinguishable: when the two gate voltages are the same (Figure 3.5a and d), the I-V is linear and quasi symmetrical; when the two gate voltages have opposite values (Figure 3.5b and c), the I-V curve is asymmetric and presents a rectifying behaviour. Therefore, in the first case the system behaves as a single gated FET, with an identical doping on both sides of the junction, while in the second case the  $p$ - $n$  junction (or diode) mode is evident.

The measurements were also performed at different temperatures (see Figure 3.6a, b and c). The asymmetry of the I-V curves under opposite gate biases ( $V_{G1} = -V_{G2} = 6$  V), computed as the ratio  $R = |I(+1V)|/|I(-1V)|$ , appears to be strongly dependent on the operating temperature (Figure 3.6d): at high temperature ( $>200$  K), the forward current is one order of magnitude larger than the reverse one. As the temperature is decreased, the current asymmetry drastically increases and reaches a factor of  $10^3$  at 150 K. Below this temperature, the I-V asymmetry decreases again. This behaviour can be connected to the two thermal contributions here at play: the thermal activation of the mobility  $E_{A,\mu}$  and the thermal activation of the carriers  $E_{A,n}$ . The former is usually one order of magnitude lower ( $\approx 10$  meV), with a significant contribution only at temperatures lower than 150 K (at 100 K,  $k_B T \approx 9$  meV).

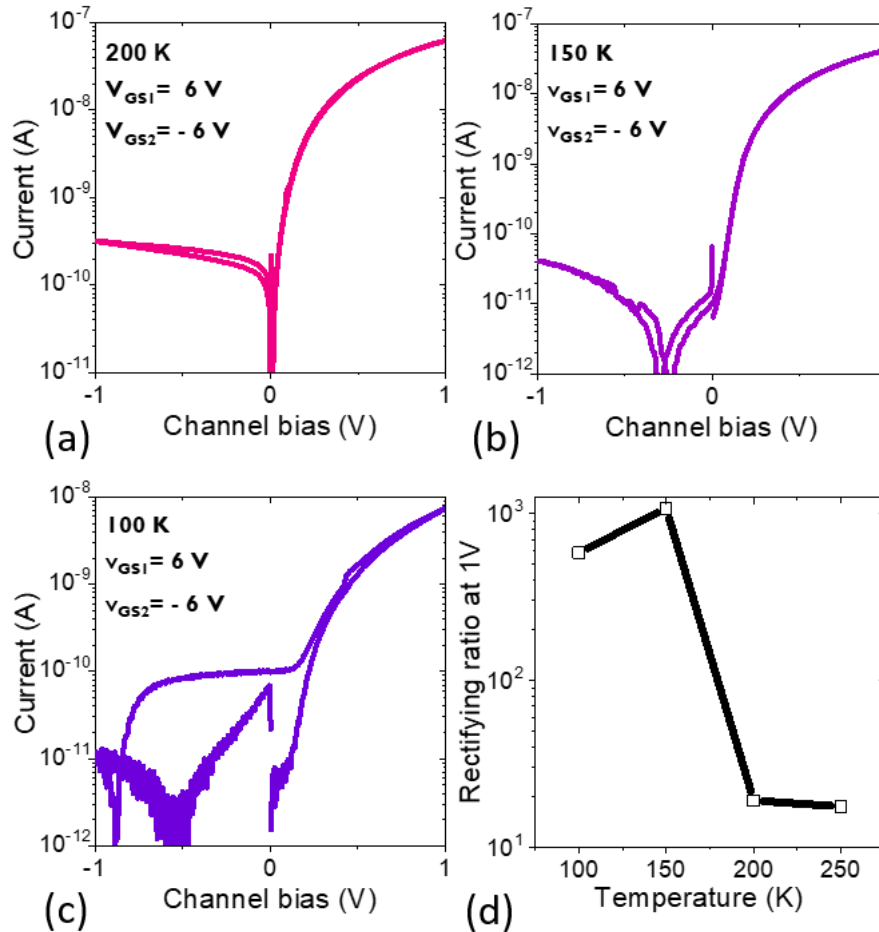


**Figure 3.6:** Temperature dependence of the I-V curves while the gate biases are opposite. a. I-V at 200 K (b at 150 K, c at 100 K). d. Rectifying ratio  $R = |I(+1V)|/|I(-1V)|$  as function of temperature.

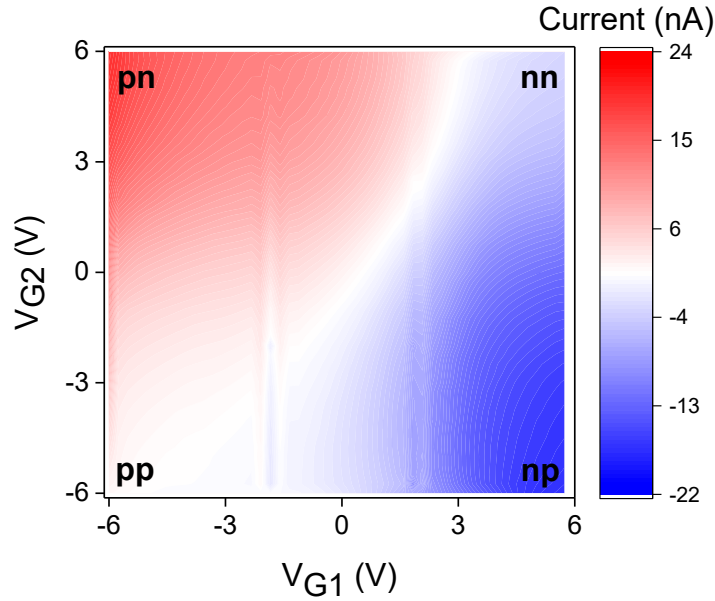


**Figure 3.7:** Photocurrent map under illumination and at 0 V channel bias.

Then, a **photocurrent map** was measured: it’s a 2D map showing the value of the current at 0 V channel bias as a function of the applied gate biases, when the device is under illumination (see [Figure 3.7](#)). It shows that in the diode mode (opposite gate biases) a photocurrent is generated at 0 V, while in the transistor mode (same gate biases) there’s no photocurrent.

Focusing on the diode operating mode of the device ( $V_{G1} = +6$  V;  $V_{G2} = -6$  V), I-V measurements were performed under illumination at different incident powers ([Figure 3.8a](#)) to observe the device behaviour in light. Illumination was provided by means of a 1.55  $\mu\text{m}$  laser diode and different incident powers were obtained by placing Neutral Density (ND) filters along its light path.

When subjected to light, the I-V characteristic is shifted and an open circuit voltage is observed ( $V_{oc}$ ). As one would expect, to increasing incident power corresponds an increasing  $V_{oc}$ .

As previously explained, it is always needed to estimate some figure of merits to be able to compare performances between different devices. The responsivity can be computed as the short-circuit current  $I_{sc}$  divided by the received power  $P$ :

$$R = \frac{I_{sc}}{P} = \frac{I_{sc}}{P_{inc} \times \frac{A}{A_{spot}}}$$

Where  $P_{inc}$  is the incident power,  $A$  is the device area (here equal to 0.01  $\text{mm}^2$ ) and  $A_{spot}$  is the laser spot size (equal to 1.6  $\text{mm}^2$ ). Responsivity values as a function of the irradiance are shown in [Figure 3.8b](#). For an irradiance of 1  $\text{mW}\cdot\text{cm}^{-2}$  the value obtained is 2  $\text{mA}\cdot\text{W}^{-1}$ . This is weaker than state of the art diodes, which reach responsivities up to 1  $\text{A}\cdot\text{W}^{-1}$  (see [Table 1](#)).

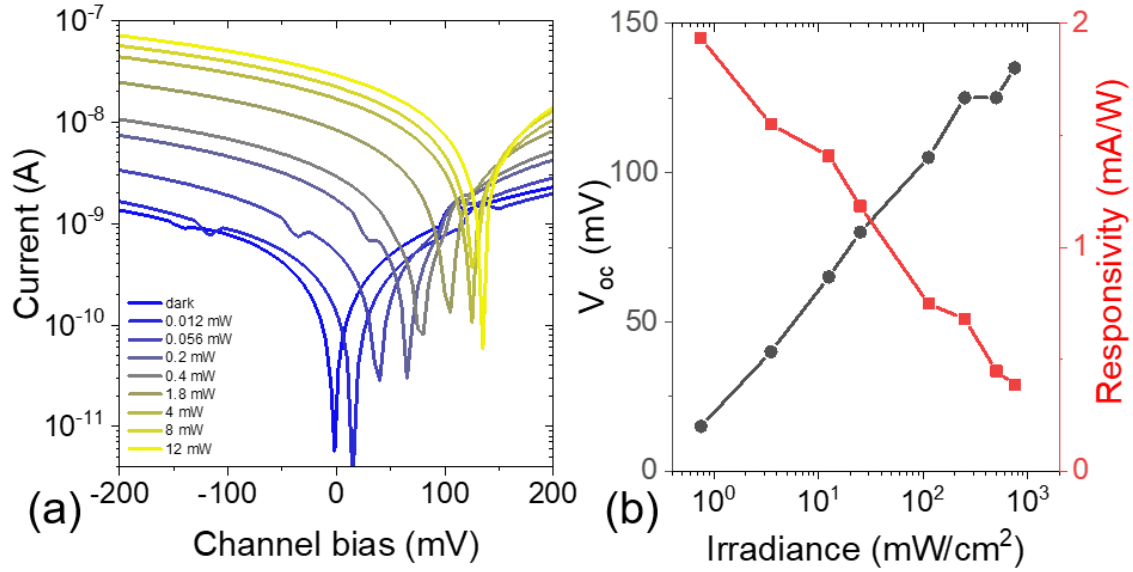


**Figure 3.8:** (a) I-V curves at different incident powers. (b)  $V_{oc}$  and Responsivity as a function of the irradiance.

### 3.2.2.3 Time-response

To measure the time-response of the sensor and see whether the geometry has allowed to achieve quicker response, time-resolved measurements are needed.

A pulsed laser (in this case a Crylas FTSS 355-50) at 355 nm is shined on the sample, with 1 ns long pulses with a 100 Hz repetition rate, giving us access to a 2 ns to 10 ms time window to resolve the device photocurrent. A GHz oscilloscope acquires the output signal, through a 50  $\Omega$  resistance.

To obtain the response in the two operating modes, one of the two gate biases ( $V_{G1}$ ) is fixed at -6 V while the other ( $V_{G2}$ ) is varied from -6 V to 6 V, with a 1 V step, at each measurement. Data processing is then needed to obtain the time response: first, the curves obtained at different gate biases are renormalized by the peak maximum, then the photocurrent decay at each gate bias is fitted by a bi-exponential function  $y = A_1 \cdot \exp(-x/t_1) + A_2 \cdot \exp(-x/t_2) + y_0$ , since a single exponential is not able to fit the overall curve (Figure 3.9a). The time response is then the  $t_1$  parameter given by the fit, which can be plotted as a function of  $V_{G2}$  (Figure 3.9b). One sees that for gate biases corresponding to the phototransistor mode, the decay time is almost 6 ns. However, when switching the operation to the diode mode, the response time reaches a value of 3 ns—the fastest reported so far for HgTe NC-based devices (see Table 1). The observed decrease in time response can be explained by an increase of the built-in electric field, *i.e.*, the internal field due to the space-charge regions, when the operation is switched to the diode mode.

Table 1 shows figures of merit for HgTe NCs-based light sensors operating in the SWIR. A useful representation of this data is presented in Figure 3.9c, a phase diagram in which the inverse of the time response is plotted as a function of the device responsivity, for devices of various geometries. The tilted grey lines correspond to the *iso-gain bandwidth product*, defined as the ratio between the responsivity and the time response.

For the split gate device, the achieved gain bandwidth product appears among the highest from literature.

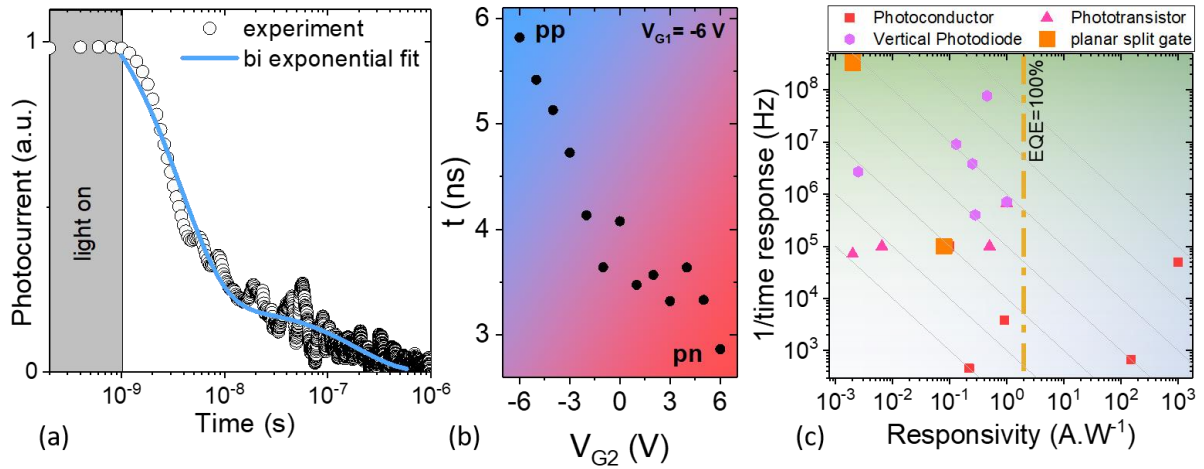


**Figure 3.9:** a. Example of fit for  $V_{G2}=-5$ V, at fixed  $V_{G1}=-6$ V. b. Time response as a function of the applied gate bias  $V_{G2}$ , at fixed  $V_{G1}=-6$ V; transistor mode coloured in blue, diode mode coloured in red. c. Inverse of the time response as a function of the responsivity of HgTe NC-based devices operated in the SWIR based on various geometries. Grey lines correspond to iso-gain bandwidth product. See Table 1 for associated references.

This new device geometry allows to obtain a fast-responding photosensor from an HgTe NC film in a dual gate FET configuration: a diode operation mode is induced by two bottom split-gates. The use of the high- $k$  dielectric makes that a  $p$ - $n$  junction can be obtained even under moderate bias operation. Coupling to graphene electrodes makes the  $p$ - $n$  junction expand within the NC film and maximizes the difference of potential between the two electrodes. The time response of the device in the diode configuration is therefore reduced down to 3 ns, resulting from a higher built-in electric field. This is fast enough to be compatible with demanding applications, such as LIDAR. Even though the device shows a weaker responsivity ( $2 \text{ mA}\cdot\text{W}^{-1}$ ) compared to state-of-the-art diodes (with responsivity up to  $1 \text{ A}\cdot\text{W}^{-1}$ ), a very competitive gain-bandwidth product is achieved.

Detectivity, an important figure of merit for photodetectors, could not be evaluated. Its estimation requires a measurement of the dark current spectral density (*i.e.*, the noise), performed with a low-frequency spectrum analyser. In this device, the electrical noise coming from the two gates prevented an accurate estimation of the noise current density.

**Table 1:** Figures of merit relative to light sensors operating in the SWIR and based on HgTe NCs (PC: photoconductor, PT: phototransistor, PD: photodiode; R: responsivity; D: detectivity; T: temperature).

Cut-off $\lambda$ ( $\mu\text{m}$ )	Operating mode	R ( $\text{A}\cdot\text{W}^{-1}$ )	Resp. time	D (J)	R/time resp.	T (K)	Specific feature	Ref.
2.5	PC	0.1	10 $\mu\text{s}$	$3.5 \times 10^{10}$	$1.0 \times 10^4$	230	As <sub>2</sub> S <sub>3</sub> surface chemistry	[7]
2.5	PC	1000	20 $\mu\text{s}$	$2 \times 10^{12}$	$5.0 \times 10^7$	200	Nanotrench	[29]

2.5	PC	150	1.5 ms	$6 \times 10^8$	$1.0 \times 10^5$	80	HgTe decorated graphene channel	[30]
2.4	PC	0.9	264 $\mu$ s decay time	$8 \times 10^9$	$3.4 \times 10^3$	300	Spray coating with patterning	[31]
2.4	PC	0.22	2.2 ms	$3.5 \times 10^8$	$1.0 \times 10^2$	300	Multicolor pixel	[32]
2.5	PT	$6.5 \times 10^{-3}$	10 $\mu$ s	$10^9$	$6.5 \times 10^2$	220	Graphene electrode	[12]
2.5	PT	$2.0 \times 10^{-3}$	14 $\mu$ s	$10^{12}$	$1.4 \times 10^2$	30	STO gate + resonator	[33]
2	PT	<0.5	$\approx 10$ $\mu$ s	$3 \times 10^{10}$	$5.0 \times 10^4$	300	SiO <sub>2</sub> back gate	[34]
2.4	PT	1	1.5 $\mu$ s	$10^{10}$	$6.7 \times 10^5$	300	Hybrid Polymer: HgTe	[35]
2.5	PT	-	15 ms	-	-	300	Doped-graphene/HgTe	[36]
2.5	PD	$2.5 \times 10^{-3}$	370 ns	$3 \times 10^9$	$6.8 \times 10^3$	300	HgTe ink	[21]
2.5	PD	0.25	260 ns decay time	$3 \times 10^{10}$ (without cavity) $7.5 \times 10^{10}$ (with cavity)	$9.6 \times 10^5$ decay time	300	Flexible substrate	[37]
2.2	PD	1	1.4 $\mu$ s decay time	$6 \times 10^{10}$	$7.1 \times 10^5$ decay time	300	HgCl <sub>2</sub> treatment	[38]
1.8	PD	0.13	110 ns	$2 \times 10^{10}$	$1.2 \times 10^6$	300	With resonator	[25]
2.5	PD	0.6	-	$4 \times 10^{11}$	-	85	Resonator grating + Fabry Perot	[39]
2.4	PD	0.45	13 ns	$10^{10}$	$3.5 \times 10^7$	300	Si/graphene/HgTe	[40]
2.5	PD	0.28	2.5 $\mu$ s	$6 \times 10^{10}$	$1.1 \times 10^5$	300	Bi <sub>2</sub> Se <sub>3</sub> /HgTe/Ag <sub>2</sub> Te	[41]
2.5	PD	0.08	10 $\mu$ s	$>10^8$ $<10^{10}$	$8.0 \times 10^3$	250	Split Gates Metallic electrode	[28]
<b>2.5</b>	PD	$2.0 \times 10^{-3}$	3 ns		$6.6 \times 10^5$	250	Split Gates Graphene electrode	<b>This device</b>

## 4 Conclusion and perspectives

The report was focused on the fabrication and characterization of one particular device geometry, conceived by the team with the purpose of increasing the photoresponse time—a targeted improvement in state-of-the-art devices based on HgTe NCs. Design of the device was the result of a combination of different features, with the goal of creating a  $p$ - $n$  junction and extending its charge dissociation area to the NCs film. An ambipolar film was required to have both type of carriers at the opposite sides of the junction, and graphene electrodes were needed for their transparency to the gate-induced electric field generating the  $p$ - $n$  junction. Through device characterization, two operating modes were demonstrated: a phototransistor mode, with a fast response time of 6 ns, and a photodiode mode, with an even faster response. In particular, a time response as fast as 3 ns was measured: the fastest reported so far for an HgTe NC-based device. Even though the resulting responsivity was found to be much weaker than other photodiodes, a very competitive gain-bandwidth product was achieved. Nevertheless, nearby perspectives in this geometry should include improvement of the device light absorption.

As for what concerns the internship activity, during the time spent at the laboratory I have had many other contributions.

The training involved device characterization, which allowed me to characterize completely the device presented in here, but also to work on other devices side by side with members of the team. Additionally, I was trained in clean room fabrication focused on UV lithographic processes: by the first month of the internship, I was able to perform alone a full UV lithographic process on ITO/FTO substrates, which are at the basis of the fabrication of vertical photodiodes—one of the many device geometries explored by the team. Moreover, I learned how to perform NCs syntheses, followed by a training on how to carry out ligand exchange procedures, both in the solid and liquid phases, and spin-coating to fabricate the NCs films. Glove box processing was also needed to carry out electrolyte gating of FETs. A good part of the activity was also spent on XPS data analysis: X-Ray Photoemission Spectroscopy measurements, performed at Synchrotron SOLEIL, are needed to analyse the electronic structure of the samples. Data analysis required peaks identification and fitting, which I performed for a few samples.

On the whole, this internship has given me the opportunity to deepen my knowledge on subjects which were addressed during my master's courses and most importantly on sensors, a topic which has always fascinated me.

## Bibliography

- [1] C. Gréboval, A. Chu, N. Goubet, C. Livache, S. Ithurria, E. Lhuillier, *Chem. Rev.* **2021**, *121*, 3627.
- [2] N. Goubet, A. Jagtap, C. Livache, B. Martinez, H. Portalès, X. Z. Xu, R. P. S. M. Lobo, B. Dubertret, E. Lhuillier, *J. Am. Chem. Soc.* **2018**, *140*, 5033.
- [3] S. E. Keuleyan, P. Guyot-Sionnest, C. Delerue, G. Allan, *ACS Nano* **2014**, *8*, 8676.
- [4] Y. Prado, J. Qu, C. Gréboval, C. Dabard, P. Rastogi, A. Chu, A. Khalili, X. Z. Xu, C. Delerue, S. Ithurria, E. Lhuillier, *Chem. Mater.* **2021**, *33*, 2054.
- [5] M. Chen, X. Lan, X. Tang, Y. Wang, M. H. Hudson, D. V. Talapin, P. Guyot-Sionnest, *ACS Photonics* **2019**, *6*, 2358.
- [6] E. Lhuillier, M. Scarafagio, P. Hease, B. Nadal, H. Aubin, X. Z. Xu, N. Lequeux, G. Patriarche, S. Ithurria, B. Dubertret, *Nano Lett.* **2016**, *16*, 1282.
- [7] E. Lhuillier, S. Keuleyan, P. Zolotavin, P. Guyot-Sionnest, *Advanced Materials* **2013**, *25*, 137.
- [8] A. Chu, C. Gréboval, N. Goubet, B. Martinez, C. Livache, J. Qu, P. Rastogi, F. A. Bresciani, Y. Prado, S. Suffit, S. Ithurria, G. Vincent, E. Lhuillier, *ACS Photonics* **2019**, *6*, 2553.
- [9] A. Jagtap, B. Martinez, N. Goubet, A. Chu, C. Livache, C. Gréboval, J. Ramade, D. Amelot, P. Troussset, A. Triboulin, S. Ithurria, M. G. Silly, B. Dubertret, E. Lhuillier, *ACS Photonics* **2018**, *5*, 4569.
- [10] P. Rastogi, A. Chu, T. H. Dang, Y. Prado, C. Gréboval, J. Qu, C. Dabard, A. Khalili, E. Dandeu, B. Fix, X. Z. Xu, S. Ithurria, G. Vincent, B. Gallas, E. Lhuillier, *Advanced Optical Materials* **2021**, *9*, 2002066.
- [11] C. Gréboval, U. N. Noubé, A. Chu, Y. Prado, A. Khalili, C. Dabard, T. H. Dang, S. Colis, J. Chaste, A. Ouerghi, J.-F. Dayen, E. Lhuillier, *Appl. Phys. Lett.* **2020**, *117*, 251104.
- [12] U. N. Noubé, C. Gréboval, C. Livache, A. Chu, H. Majjad, L. E. Parra López, L. D. N. Mouafo, B. Doudin, S. Berciaud, J. Chaste, A. Ouerghi, E. Lhuillier, J.-F. Dayen, *ACS Nano* **2020**, *14*, 4567.
- [13] G. Konstantatos, M. Badioli, L. Gaudreau, J. Osmond, M. Bernechea, F. P. G. de Arquer, F. Gatti, F. H. L. Koppens, *Nature Nanotechnology* **2012**, *7*, 363.
- [14] C. B. Murray, D. J. Norris, M. G. Bawendi, *J. Am. Chem. Soc.* **1993**, *115*, 8706.
- [15] S. Keuleyan, E. Lhuillier, P. Guyot-Sionnest, *J. Am. Chem. Soc.* **2011**, *133*, 16422.
- [16] M. A. Boles, D. Ling, T. Hyeon, D. V. Talapin, *Nature Mater* **2016**, *15*, 141.
- [17] P. Guyot-Sionnest, *J. Phys. Chem. Lett.* **2012**, *3*, 1169.
- [18] Y. Liu, M. Gibbs, J. Puthussery, S. Gaik, R. Ihly, H. W. Hillhouse, M. Law, *Nano Lett.* **2010**, *10*, 1960.
- [19] M. V. Kovalenko, M. Scheele, D. V. Talapin, *Science* **2009**, *324*, 1417.
- [20] A. Nag, M. V. Kovalenko, J.-S. Lee, W. Liu, B. Spokoyny, D. V. Talapin, *J. Am. Chem. Soc.* **2011**, *133*, 10612.
- [21] B. Martinez, J. Ramade, C. Livache, N. Goubet, A. Chu, C. Gréboval, J. Qu, W. L. Watkins, L. Becerra, E. Dandeu, J. L. Fave, C. Méthivier, E. Lacaze, E. Lhuillier, *Advanced Optical Materials* **2019**, *7*, 1900348.
- [22] S. H. Kim, K. Hong, W. Xie, K. H. Lee, S. Zhang, T. P. Lodge, C. D. Frisbie, *Adv. Mater.* **2013**, *25*, 1822.
- [23] E. Lhuillier, S. Ithurria, A. Descamps-Mandine, T. Douillard, R. Castaing, X. Z. Xu, P.-L. Taberna, P. Simon, H. Aubin, B. Dubertret, *J. Phys. Chem. C* **2015**, *119*, 21795.

- [24] C. Gréboval, U. Noumbe, N. Goubet, C. Livache, J. Ramade, J. Qu, A. Chu, B. Martinez, Y. Prado, S. Ithurria, A. Ouerghi, H. Aubin, J.-F. Dayen, E. Lhuillier, *Nano Lett.* **2019**, *19*, 3981.
- [25] P. Rastogi, A. Chu, T. H. Dang, Y. Prado, C. Gréboval, J. Qu, C. Dabard, A. Khalili, E. Dandeu, B. Fix, X. Z. Xu, S. Ithurria, G. Vincent, B. Gallas, E. Lhuillier, *Advanced Optical Materials* **2021**, 2002066.
- [26] G. Konstantatos, E. H. Sargent, *Appl. Phys. Lett.* **2007**, *91*, 173505.
- [27] X. Tang, K. W. C. Lai, *ACS Appl. Nano Mater.* **2019**, *2*, 6701.
- [28] S.-S. Chee, C. Gréboval, D. V. Magalhaes, J. Ramade, A. Chu, J. Qu, P. Rastogi, A. Khalili, T. H. Dang, C. Dabard, Y. Prado, G. Patriarche, J. Chaste, M. Rosticher, S. Bals, C. Delerue, E. Lhuillier, *Nano Lett.* **2021**, *21*, 4145.
- [29] A. Chu, C. Gréboval, Y. Prado, H. Majjad, C. Delerue, J.-F. Dayen, G. Vincent, E. Lhuillier, *Nature Communications* **2021**, *12*, 1794.
- [30] M. J. Grotevent, C. U. Hail, S. Yakunin, D. Bachmann, M. Calame, D. Poulikakos, M. V. Kovalenko, I. Shorubalko, *Advanced Science* **2021**, *8*, 2003360.
- [31] M. E. Cryer, J. E. Halpert, *ACS Photonics* **2018**, *5*, 3009.
- [32] M. E. Cryer, L. A. Browning, N. O. V. Plank, J. E. Halpert, *ACS Photonics* **2020**, *7*, 3078.
- [33] C. Gréboval, A. Chu, D. V. Magalhaes, J. Ramade, J. Qu, P. Rastogi, A. Khalili, S.-S. Chee, H. Aubin, G. Vincent, S. Bals, C. Delerue, E. Lhuillier, *ACS Photonics* **2021**, *8*, 259.
- [34] M. Chen, H. Lu, N. M. Abdelazim, Y. Zhu, Z. Wang, W. Ren, S. V. Kershaw, A. L. Rogach, N. Zhao, *ACS Nano* **2017**, *11*, 5614.
- [35] Y. Dong, M. Chen, W. K. Yiu, Q. Zhu, G. Zhou, S. V. Kershaw, N. Ke, C. P. Wong, A. L. Rogach, N. Zhao, *Adv. Sci.* **2020**, *7*, 2000068.
- [36] X. Tang, K. W. C. Lai, *ACS Appl. Nano Mater.* **2019**, *2*, 6701.
- [37] X. Tang, M. M. Ackerman, G. Shen, P. Guyot-Sionnest, *Small* **2019**, *15*, 1804920.
- [38] M. M. Ackerman, M. Chen, P. Guyot-Sionnest, *Appl. Phys. Lett.* **2020**, *116*, 083502.
- [39] X. Tang, M. M. Ackerman, P. Guyot-Sionnest, *ACS Nano* **2018**, *12*, 7362.
- [40] X. Tang, M. Chen, A. Kamath, M. M. Ackerman, P. Guyot-Sionnest, *ACS Photonics* **2020**, *7*, 1117.
- [41] X. Tang, M. M. Ackerman, M. Chen, P. Guyot-Sionnest, *Nature Photonics* **2019**, *13*, 277.